

IRAS 23385+6053: A Prototype Massive Class 0 Object⁰

Sergio Molinari ¹, Leonardo Testi ², Jan Brand ³, Riccardo Cesaroni ⁴ and Francesco Palla ⁴

ABSTRACT

IRAS 23385+6053 is a Young Stellar Object with luminosity $\sim 1.6 \times 10^4 L_{\odot}$ at a kinematic distance of 4.9 kpc. This candidate precursor of an ultracompact HII region is associated with a millimeter source detected at the JCMT but is undetected at centimeter wavelengths with the VLA. We observed this source with the OVRO millimeter array at 3.4 mm in the continuum, $\text{HCO}^+(1 \rightarrow 0)$, $\text{H}^{13}\text{CO}^+(1 \rightarrow 0)$ and $\text{SiO}(v=0, 2 \rightarrow 1)$ line emission, and with CAM aboard ISO at $6.75\mu\text{m}$ and $15\mu\text{m}$. The IRAS source is coincident with a 3.4 mm compact ($r_{\text{core}} \simeq 0.048$ pc) and massive ($M \simeq 370 M_{\odot}$) core, which is undetected at $15\mu\text{m}$ to a 3σ level of 6 mJy; this is compatible with the derived H_2 column density of $\sim 2 \times 10^{24} \text{cm}^{-2}$ and the estimated visual extinction $A_V \sim 2000$ mag. We find $L_{\text{submm}}/L_{\text{bol}} \sim 3 \times 10^{-3}$ and $M_{\text{env}}/M_{\star} \gg 1$, typical of Class 0 objects. The source is also associated with a compact outflow characterized by a size $\lesssim r_{\text{core}}$, a dynamical timescale of $\lesssim 7 \times 10^3$ years, and a mass loss rate $\dot{M} \gtrsim 10^{-3} M_{\odot} \text{yr}^{-1}$. The axis of the outflow is oriented nearly perpendicular to the plane of the sky, ruling out the possibility that the non-detection at $15 \mu\text{m}$ is the result of a geometric effect. All these properties suggest that IRAS 23385+6053 is the first example of a *bona fide* massive Class 0 object.

Subject headings: infrared: ISM : continuum — ISM: individual (IRAS 23385+6053) — ISM: jets and outflows — ISM: molecules — radio continuum: ISM — radio lines: ISM — stars: formation

⁰Based on observations with ISO, an ESA project with instruments funded by ESA Member States (especially the PI countries: France, Germany, the Netherlands and the United Kingdom) with the participation of ISAS and NASA.

¹Infrared Processing and Analysis Center, California Institute of Technology, MS 100-22, Pasadena, CA 91125 (molinari@ipac.caltech.edu)

²Division of Physics, Mathematics and Astronomy, California Institute of Technology, MS 105-24, Pasadena, CA 91125 (lt@astro.caltech.edu)

³Istituto di Radioastronomia - CNR, Via Gobetti 101, I-40129, Bologna (brand@astbo1.bo.cnr.it)

⁴Osservatorio Astrofisico di Arcetri, Largo E. Fermi 5, I-50125, Firenze (palla, cesa@arcetri.astro.it)

1. Introduction

The last few years have seen a rapid growth in observations aimed at identifying intermediate- and high-mass star forming sites in a wide range of evolutionary stages ranging from “Hot Cores” (Cesaroni et al. 1994), to ultracompact HII (UCHII) regions (Wood & Churchwell 1989), to proto-Ae/Be stars (Hunter et al. 1998). The characterization of the earliest stages of high mass-star formation is more difficult than for low-mass objects, given their shorter evolutionary timescales. The likely candidates must be luminous, embedded in dense circumstellar environments, and non-associated with HII regions (c.f. Habing & Israel 1979)

We have undertaken a systematic study to identify a sample of massive protostellar candidates, selecting sources from the IRAS-PSC2 catalogue and filtering them according to the above criteria. On the basis of H₂O maser (Palla et al. 1991), ammonia lines (Molinari et al. 1996), centimeter and submillimeter continuum observations (Molinari et al. 1998a; 1998b), we were finally left with about a dozen candidates which may be precursors of UCHII regions. Several of these sources have been recently observed with the IRAM-30m telescope (Brand et al. 1998, in preparation) and some with the Infrared Space Observatory (ISO), to characterize them over a wide range of wavelengths. We are now beginning a program of high spatial resolution millimeter wave observations of these objects. This *Letter* presents the results for the first source imaged, IRAS 23385+6053, at a kinematic distance ¹ of 4.9 kpc (using the Brand & Blitz (1993) galactic rotation curve). According to the definition (e.g. André 1996), this is an excellent candidate of a high-mass counterpart of Class 0 objects. It is associated with an H₂O maser and with NH₃ line and submillimeter continuum emission, while no centimeter continuum emission was detected in our VLA observations down to a level of ~ 0.5 mJy/beam.

2. Observations

The field centered on IRAS 23385+6053 was observed at 88 GHz (continuum and lines) with the Owens Valley Radio Observatory (OVRO) millimeter wave array during January/February 1998. Two configurations of the six 10.4-m telescope antennas provided baselines in the range 15–240 m. Cryogenically cooled SIS receivers have typical average system temperature of ~ 350 K. The continuum observations used two 1 GHz wide

¹In Molinari et al. (1996), we quoted a distance of 6.9 kpc derived from the *observed* galactic velocity field, which should however not be used for $d \geq 5$ kpc in the 2nd and 3rd quadrants.

bands of an analog correlator. For the line observations, the digital correlator was split into several bands, enabling simultaneous observations of the $\text{HCO}^+(1 \rightarrow 0)$ and $\text{H}^{13}\text{CO}^+(1 \rightarrow 0)$ rotational lines with $\sim 20 \text{ km s}^{-1}$ bandwidth and 0.84 km s^{-1} resolution; the $\text{HCO}^+(1 \rightarrow 0)$ line was also observed with a $\sim 80 \text{ km s}^{-1}$ bandwidth and 3.4 km s^{-1} resolution. Additionally, data on the $\text{SiO}(v=0, 2 \rightarrow 1)$ line were acquired in the image sideband of the $\text{HCO}^+(1 \rightarrow 0)$ line with the same bandwidths and resolutions. Gain and phase were calibrated by means of frequent observations of the quasar 0224+671. 3C273 was used for passband calibration. The flux density scale was determined by observations of planets and the estimated uncertainty is less than 20%. The synthesized beamsize is $4''.1 \times 3''.5$. Noise levels in the maps are $\sim 0.7 \text{ mJy/beam}$, $\sim 20 \text{ mJy/beam}$, and $\sim 45 \text{ mJy/beam}$ for the continuum and the low and high resolution spectral data, respectively.

ISO (Kessler et al. 1996) observations with CAM (Cesarsky et al. 1996) were made in staring mode on June 18 1997. Diffraction-limited images (resolution $2''.2$ and $5''$, respectively) were obtained in the two broad-band filters LW2 ($\lambda_{eff}=6.75\mu\text{m}$, $\Delta\lambda=3.5\mu\text{m}$) and LW3 ($\lambda_{eff}=15.0\mu\text{m}$, $\Delta\lambda=6\mu\text{m}$). The pixel-field-of-view is $3''$, and the absolute pointing accuracy of the satellite was presumably within $\sim 3''$ at the time of the observations. More than 50 frames per filter were obtained with a 2s integration time per frame, and the expected 3σ sensitivity limits were 0.33 and $0.45 \text{ mJy/arcsec}^2$ in LW2 and LW3, respectively. The data have been reduced using CAM Interactive Analysis (V2.0), and the absolute calibration is accurate within 20%.

3. Results

Figure 1a shows the contour plot of the $\text{HCO}^+(1 \rightarrow 0)$ integrated line intensity overlaid on the CAM-LW3 filter $15 \mu\text{m}$ image. Figure 1b shows an enlargement of the central region, with a contour plot of the 3.4 mm continuum. With the exception of $\text{HCO}^+(1 \rightarrow 0)$ emission in one area to the NE, the HCO^+ line and the 3.4 mm continuum arise from the central region where the $15 \mu\text{m}$ continuum is faintest; HCO^+ also shows an extension towards S-SE.

In the dark region at the center of the $15 \mu\text{m}$ image, flux densities of the order of $\sim 1 \text{ mJy/arcsec}^2$ are found. Similar values are also found in the southern portion of the CAM field, suggesting that such a constant level is due to faint foreground diffuse emission. The *rms* noise computed in the southern $20''$ of the image is $\sim 0.15 \text{ mJy/arcsec}^2$. Similar flux densities and *rms* levels are obtained for the $6.75 \mu\text{m}$ image. We thus conclude that no $15 \mu\text{m}$ source is detected at the position of the central 3.4 mm continuum peak down to a

3σ level of ~ 0.45 mJy/arcsec² which, integrated over the deconvolved area of the 3.4 mm core, corresponds to ~ 6 mJy.

The 3.4 mm continuum core is compact with slight elongations to the SE and N (Fig. 1). The total integrated flux density is 19 mJy and the deconvolved source size is $4''.5 \times 3''.6$, corresponding to an average radius of 0.048 pc at a distance of 4.9 kpc. The continuum emission peaks at $\alpha(1950) = 23^h38^m31^s.4$, $\delta(1950) = +60^\circ53'50''$, and is probably due solely to dust thermal emission since the extrapolation at 3.4 mm of the 2 cm upper limit with an ionized wind model $\sim \nu^{0.6}$ (Panagia & Felli 1975) yields less than 10% of the observed flux density.

Fig. 2 shows the complete spectral energy distribution (SED) of IRAS 23385+6053. The OVRO flux density is consistent with those from JCMT (Molinari et al. 1998b), indicating that no significant diffuse millimeter emission has been missed by the interferometer. On the other hand the IRAS flux densities include contributions of all the sources seen in the 15 μ m image of Fig. 1. Indeed, the IRAS 12 μ m and 25 μ m points in Fig. 2 (5.05 and 17.8 Jy, respectively) are compatible with the CAM 6.75 and 15 μ m flux integrated over all the bright emission visible on the CAM image (~ 4.8 and 9.3 Jy respectively, in an area of 6.8×10^{-8} sterad), while they lie more than 3 orders of magnitude above the CAM flux density limits for the core estimated above. Clearly, the 6.75 and 15 μ m emission area, which is not directly related to the millimeter core, is responsible for the IRAS 12 and 25 μ m flux densities; however, it is unlikely that it contributes for a significant fraction of the 60 μ m and 100 μ m IRAS flux densities because: 1) at millimeter wavelengths, the core is compact and no discrete or diffuse continuum emission is detected at either OVRO or the JCMT; 2) a power law extrapolation of the 6.75, 12, 15 and 25 μ m flux densities to longer wavelengths, leads to flux densities at 60 and 100 μ m $\lesssim 10\%$ of the observed values. We conclude that the millimeter core is the only source contributing significantly at 60 and 100 μ m.

In Fig. 2 the dotted line is a fit to the data, obtained adopting a spherical envelope model where density and temperature vary according to radial power laws with exponents -0.5 and -0.4 respectively. The density and temperature at the external radius, which is the observed $r_{core} \simeq 0.048$ pc, are 7×10^6 cm⁻³ and 40 K. The opacity is $\kappa_\nu = \kappa_{1.3mm} (\lambda(\text{mm})/1.3)^{-1.9}$, $\kappa_{1.3mm} = 0.005$ cm² g⁻¹ (Preibisch et al. 1993). We compute the bolometric luminosity of the source by integrating the data with a power law interpolation scheme, excluding the IRAS 12 and 25 μ m flux densities and using the CAM upper limit at 15 μ m. At the adopted distance of 4.9 kpc, we find $L_{bol} \simeq 1.6 \times 10^4 L_\odot$. Integrating the fitted density power law and adopting a gas to dust ratio of 100 by mass, we estimate a mass of $\sim 370 M_\odot$ and a mean H₂ column density of $\sim 2 \times 10^{24}$ cm⁻² for the core (corresponding to a visual

extinction $A_V \sim 2000$). We also computed the mass of the core from HCO^+ line emission. The optical depth in each channel within 3 km s^{-1} of $V_{LSR} = -51 \text{ km s}^{-1}$ was estimated from the $\text{HCO}^+/\text{H}^{13}\text{CO}^+$ ratio, assuming a $^{12}\text{C}/^{13}\text{C} = 87$ abundance ratio using the galactic abundance gradient and the local-ISM value given in Wilson & Rood (1994) and a source galactocentric distance of $\sim 11 \text{ kpc}$; we find that the core of the main isotope line is optically thick. We derive a lower limit (due to the optical depth) for the H_2 mass of $180 M_\odot$ assuming $T_{ex} = 30 \text{ K}$, based on the peak $\text{HCO}^+(1 \rightarrow 0)$ synthesized beam brightness temperature, and $[\text{HCO}^+]/[\text{H}_2] = 10^{-9}$. This value compares reasonably well with a virial mass of $160 M_\odot$ obtained from the line width ($\sim 3.5 \text{ km s}^{-1}$) and $\text{HCO}^+(1 \rightarrow 0)$ core radius ($\sim 0.06 \text{ pc}$).

In Fig. 3 we present profiles of the $\text{SiO}(v=0, 2 \rightarrow 1)$ and $\text{HCO}^+(1 \rightarrow 0)$ lines at low spectral resolution and the $\text{HCO}^+(1 \rightarrow 0)$ and $\text{H}^{13}\text{CO}^+(1 \rightarrow 0)$ lines at higher resolution, integrated over the $\sim 20 \text{ arcsec}^2$ centered on the core peak. Both the SiO and the HCO^+ profiles show broad wings, while no wing emission is detected from $\text{H}^{13}\text{CO}^+(1 \rightarrow 0)$. Images of the HCO^+ and SiO emission integrated over the blue (from -63 to -53 km s^{-1}) and the red (from -47 to -37 km s^{-1}) wings are shown in Fig. 4. A compact outflow centered on the continuum source is detected; both the blue and the red lobes are visible in $\text{SiO}(v=0, 2 \rightarrow 1)$, whereas only the blue lobe is clearly detected in $\text{HCO}^+(1 \rightarrow 0)$, although a faint red lobe may be present. The lobes are barely resolved; their position relative to each other, i.e. their degree of overlap, suggests that the inclination of its axis can be no more than 30° with respect to the line of sight (Cabrit & Bertout 1986; 1990). This orientation of the outflow rules out any possibility that the large extinction derived toward IRAS 23385+6053 and the non-detection at $15 \mu\text{m}$ may result from geometrical effects (e.g. an edge-on disk). Properties of the IRAS 23385+6053 outflow are listed in Table 1. Column density, mass, momentum and energy are computed in each velocity channel and finally summed, while the dynamical timescale is averaged over the velocity channels. We estimated the column density of material assuming LTE and optically thin approximations in all the line wings channels within the velocity ranges listed previously, assuming the above determined excitation temperature of 30 K for both HCO^+ and SiO . For both molecules we adopt an abundance fraction of 10^{-9} relative to H_2 . The velocity measured in the lobes is a good estimate of the true gas velocity because the outflow axis is nearly perpendicular to the plane of the sky. This configuration prevents an accurate measure of lobe size, but a reasonable estimate can be made based on the non-detection at $15 \mu\text{m}$. Since any outflow more extended than the core would have created a cavity through which mid-infrared radiation could have escaped, we infer that the extent of the flow lobes is less than the core size. The size of the lobes and the dynamical time scale of the outflow are therefore upper limits, while the mass loss rate and kinetic luminosity are lower limits.

The flow mechanical power and mass loss rate in Table 1 are high compared to values characterizing outflows powered by low-mass protostars (e.g. Fukui et al. 1993), but in good agreement with those for high-mass young stellar objects (Shepherd & Churchwell 1996). Nevertheless, the dynamical timescale is similar to values found for the youngest outflows around low-mass Class 0 objects (André et al. 1993).

4. IRAS 23385+6053: A Massive Class 0 Object

IRAS 23385+6053 was not detected at 6 and 2 cm with the VLA B-array with 3σ sensitivity limits of ~ 0.5 and ~ 0.8 mJy/beam respectively (Molinari et al. 1998a), implying that any associated HII region, if present, must be optically thick and very compact. In this latter case, from the VLA synthesized beamsizes and assuming that the source has not been detected because of beam dilution, the 2 cm upper limit leads to an upper limit for the radius of an optically thick, spherical and homogeneous HII region $r_{\text{HII}} \lesssim 100$ AU (see also Molinari et al. 1998a). An HII region originating from a B0 ZAMS star (which has a luminosity comparable to the bolometric luminosity of IRAS 23385+6053) in a dense ($n_{\text{H}_2} \sim 10^7 \text{ cm}^{-3}$) environment takes only few years to expand to a radius of 100 AU (De Pree et al. 1995). However, a modest accretion rate of $4 \times 10^{-6} M_{\odot}/\text{yr}$ could squelch the expanding HII region (see e.g. Walmsley 1995), thus explaining the properties of our source in terms of a heavily obscured B0-ZAMS with a residual accretion. Another possible explanation is that there is no HII region because IRAS 23385+6053 has not yet reached the ZAMS. In this case we assume that the observed bolometric luminosity is due to accretion onto a protostellar core with accretion luminosity expressed as $L_{\text{acc}} = 3.14 \times 10^4 L_{\odot} (M_{\star}/M_{\odot}) (R_{\odot}/R_{\star}) (\dot{M}/10^{-3} M_{\odot} \text{ yr}^{-1})$. Since L_{acc} is known, we can combine it with the mass-radius relation of Stahler, Palla & Salpeter (1986), $R_{\star} = 27.2 \times R_{\odot} (M_{\star}/M_{\odot})^{0.27} (\dot{M}/10^{-3} M_{\odot} \text{ yr}^{-1})^{0.41}$, to derive the protostellar mass M_{\star} as a function of the accretion rate. For an accretion rate $\dot{M} \sim 10^{-3} M_{\odot} \text{ yr}^{-1}$, which is expected if the outflow (see Table 1) is driven by infall (e.g. Shu et al. 1988), we obtain $M_{\star} = 39 M_{\odot}$, implying that the embedded IRAS source is a massive protostar. In either case, this source is evidently massive and extremely young.

Based on the evidence presented here, *we propose IRAS 23385+6053 as a prototype high-mass Class 0 object*: it is undetected in the mid-IR ($\lambda < 15 \mu\text{m}$) and in the radio continuum; it has $L_{\text{submm}}/L_{\text{bol}} \gtrsim 5 \times 10^{-3}$ (where L_{submm} is obtained by integrating longward of $350 \mu\text{m}$); it has a ratio of the envelope to stellar mass greater than 1 (see André et al. 1993), $M_{\text{env}}/M_{\star} \gtrsim 10$. The very short dynamical timescale ($\lesssim 7000$ yrs) of the associated compact molecular outflow is also compatible with values found for outflows

around low-mass Class 0 objects.

Acknowledgements: We thank Anneila Sargent for a critical reading of the manuscript. Support from NASA's *Origins of Solar Systems* program (through grant NAGW-4030) is gratefully acknowledged. The Owens Valley millimeter-wave array is supported by NSF grant AST-96-13717. Research at Owens Valley on young star and disk systems is also supported by the *Norris Planetary Origins Project*. The ISOCAM data presented in this paper were analysed using "CIA", a joint development by the ESA Astrophysics Division and the ISOCAM Consortium. This project was partly supported by CNR grant 97.00018.CT02 and by ASI grant ARS 96-66 to the Osservatorio di Arcetri.

REFERENCES

- André, P. 1996, Mem. SAI, 67, 901
- André, P., Ward-Thompson, D., & Barsony, M. 1993, ApJ, 406, 122
- Beckwith, S. V. W., Sargent, A. I., Chini, R. S., Güsten, R. 1990, AJ, 99, 924
- Brand, J., & Blitz, L. 1993, A&A, 275, 67
- Cabrit, S. & Bertout, C. 1986, ApJ, 307, 313
- Cabrit, S. & Bertout, C. 1990, ApJ, 348, 541
- Cesaroni, R., Churchwell, E., Hofner, P., Walmsley, C. M., & Kurtz, S. 1994, A&A, 288, 903
- Cesaroni, R., Felli, M., Testi, L., Walmsley, C. M., & Olmi, L. 1997, A&A, 325, 725
- Cesarsky, C.J., Abergel, A., Agnese, P, et al. 1996, A&A, 315, L32
- De Pree, C. G., Rodríguez, L. F., & Goss, W. M. 1995, Rev. Mex. Astron. Astrophys., 31, 39
- Fukui, Y., Iwata, T., Mizuno, A., Bally, J., & Lane, A. P. 1993, Protostars & Planets III, p. 603
- Habing, H. J., & Israel, F. P. 1979, ARA&A, 17, 345
- Hildebrand, R. H. 1983, QJRAS, 24, 267

- Hunter, T. R., Neugebauer, G., Benford, D. J., Matthews, K., Lis, D. C., Serabyn, E., & Phillips, T. G. 1998, *ApJ*, 493, L97
- Kessler, M.F., Steinz, J.A., Anderegg, M.E., et al. 1996, *A&A*, 315, L27
- Molinari, S., Brand, J., Cesaroni, R., & Palla, F. 1996, *A&A*, 308, 573
- Molinari, S., Brand, J., Cesaroni, R., Palla, F., & Palumbo, G.G.C. 1998a, *A&A*, 336, 339
- Molinari, S., Brand, J., Cesaroni, R., Palla, F. 1998b, in preparation
- Palla, F., Brand, J., Cesaroni, R., Comoretto, G., & Felli, M. 1991, *A&A*, 246, 249
- Panagia, N. 1973, *AJ*, 78, 929
- Panagia, N. & Felli, M. 1975, *A&A*, 39, 1
- Preibisch, Th., Ossenkopf, V., Yorke, H.W., & Henning, Th. 1993, *A&A*, 279, 577
- Shu, F. H., Lizano, S., Ruden, S. P., & Najita, J. 1988, *ApJ*, 328, L19
- Shepherd, D. S. & Churchwell, E. 1996, *ApJ*, 457, 267
- Stahler, S. W., Palla, F., & Salpeter, E. E. 1986, *ApJ*, 302, 590
- Walmsley, C. M. 1995, *Rev. Mex. Astron. Astrof., Series de Conferencias*, 1, 137
- Wilson, T. L. & Rood, R. 1994, *ARA&A*, 32, 191
- Wood, D. O. S., & Churchwell, E. 1989, *ApJS*, 69, 831

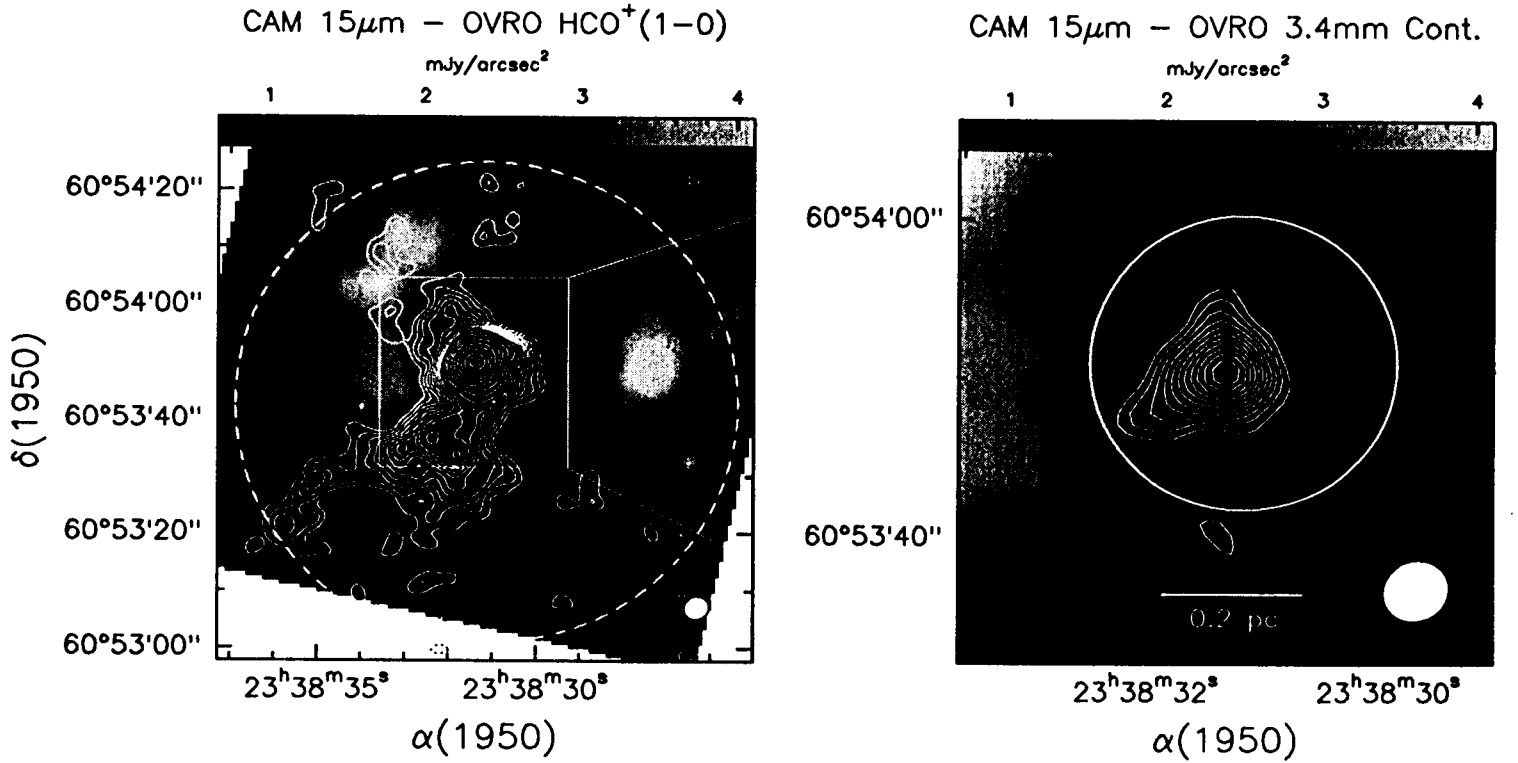


Fig. 1.— a) CAM LW3 filter (15μm) image of IRAS 23385+6053, with superposed the contour plot of HCO⁺(1 → 0) line intensity integrated over a velocity interval of ~ 7 km s⁻¹ centered at $V_{LSR} = -51.0$ km s⁻¹; the CAM image has been resampled at the same pixel size used to reconstruct the OVRO maps. To avoid saturation at the peak emission, contours are spaced from 0.3 to 1.5 by 0.15, from 1.5 to 3.0 by 0.3, and from 3.5 to 5.6 by 0.5 Jy km s⁻¹/beam. The dashed circle shows the OVRO primary beam HPBW. - b) Enlargement of the previous image around the central position with superposed the contour plot of the OVRO 3.4mm continuum emission from 2.0 to 9.0 by 0.7 mJy/beam. The circle shows the JCMT 19" aperture centered at the 1.1 mm peak position. The grey ellipse is the OVRO synthesized beam FWHP.

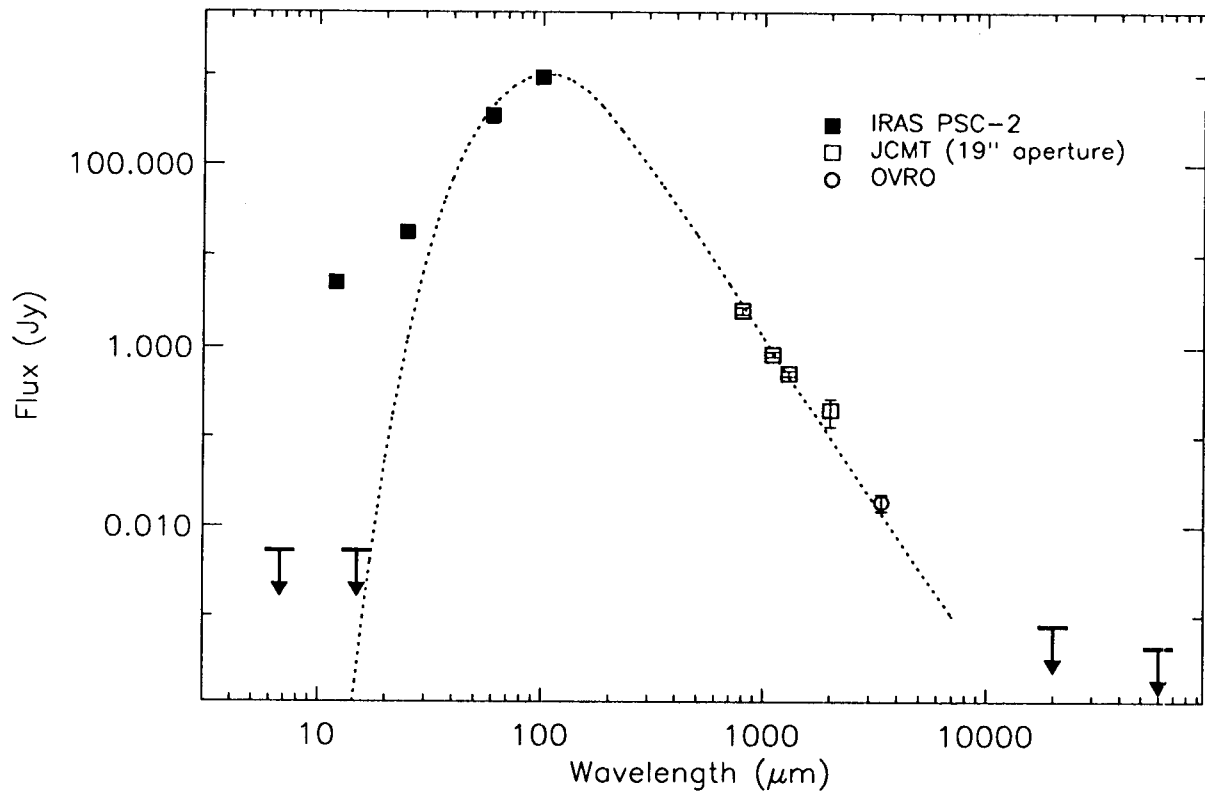


Fig. 2.— Spectral energy distribution of the IRAS 23385+6053 core. The dotted line shows the model fit described in the text.

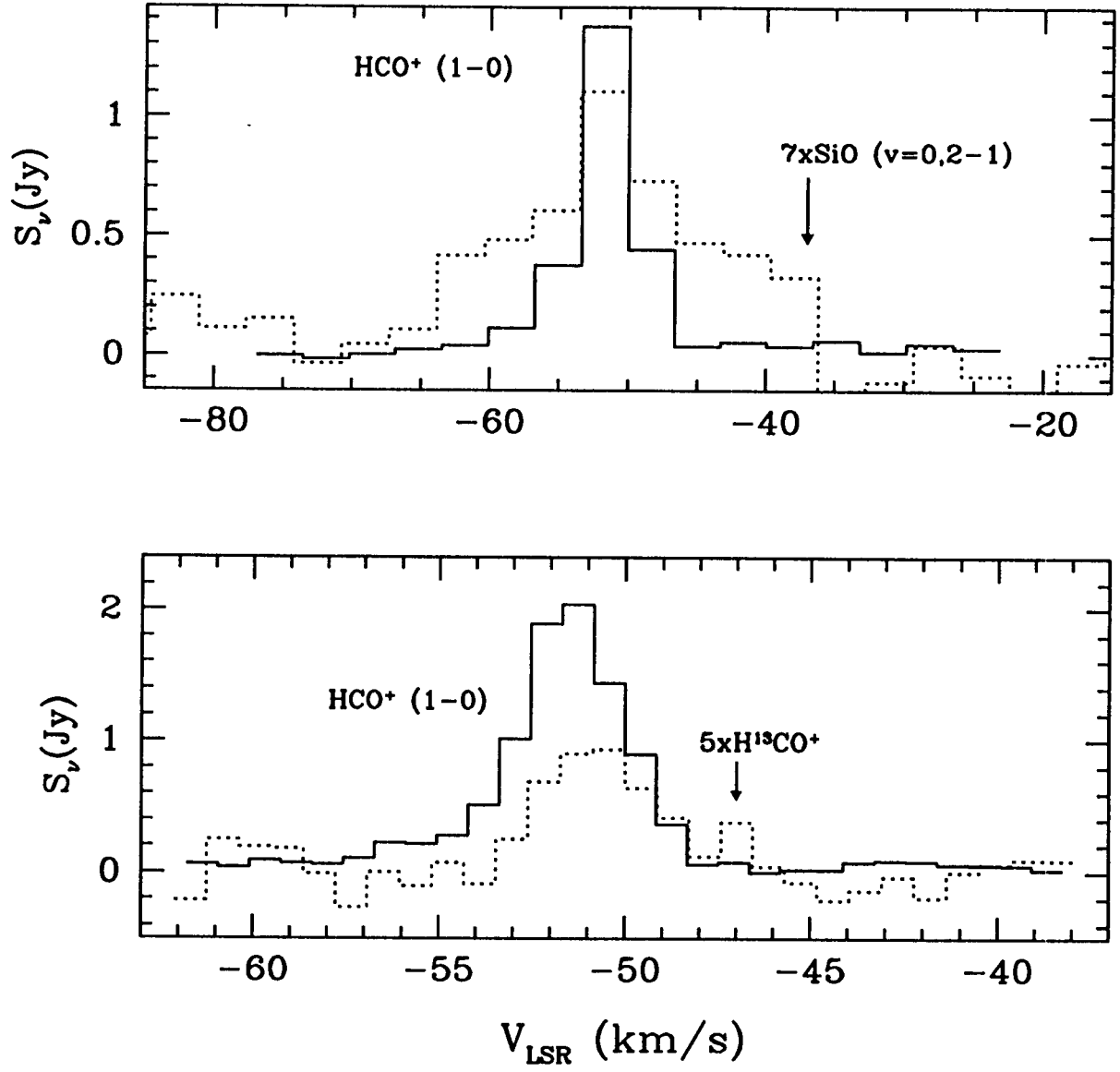


Fig. 3.— OVRO spectra integrated over $\sim 20 \text{ arcsec}^2$ area centered on the core. Top panel: low resolution, $\text{rms}=0.02 \text{ Jy}$. Bottom panel: high resolution, $\text{rms}=0.04 \text{ Jy}$. In all panels, the vertical scale is the flux density in Jansky.

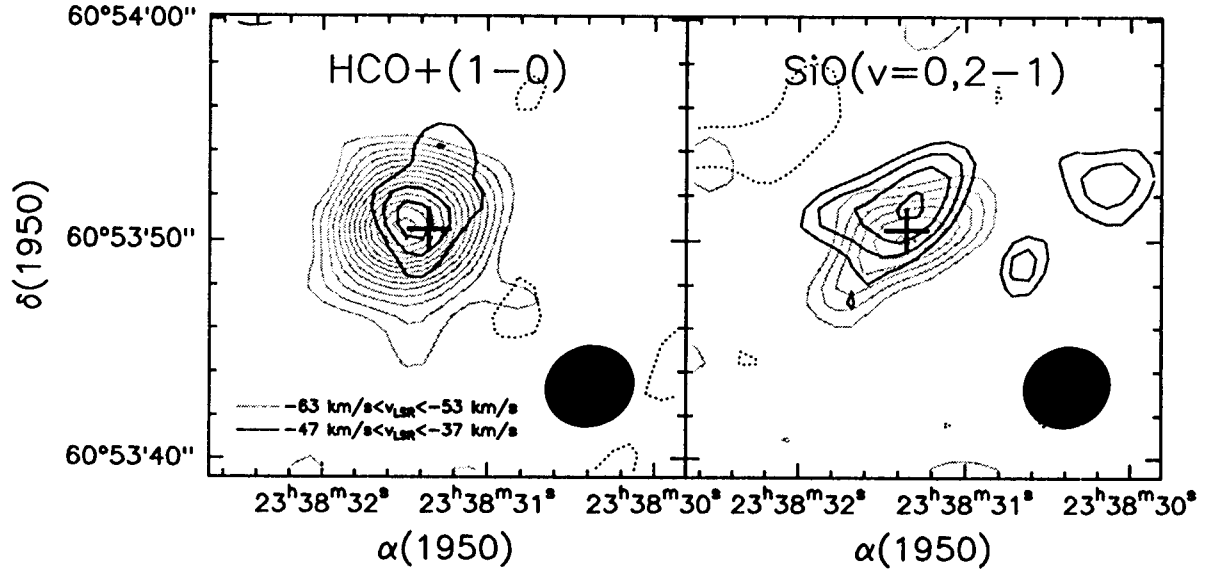


Fig. 4.— Outflow maps of IRAS 23385+6053. Contour levels start at 0.3 and increment by 0.12 Jy km s⁻¹ for the two maps; the dotted contour corresponds to -0.3 Jy km s⁻¹. The cross represents the position of the peak in the 3.4 mm continuum map. The full ellipse is the OVRO beam

Table 1. Outflow Parameters

Parameter	HCO ⁺ (1 → 0)	SiO(v=0, 2 → 1)
N _{H₂} (cm ⁻²)	7.5×10 ²²	1.4×10 ²³
M _{H₂} (M _⊙)	10.6	19.6
P = ∑ _i M _i v _i (M _⊙ km s ⁻¹)	66.6	159.6
E=½ ∑ _i M _i v _i ² (ergs)	4.7×10 ⁴⁵	1.4×10 ⁴⁶
< τ _{dyn} > (yr)	7300	5600
\dot{M} (M _⊙ yr ⁻¹)	1.5×10 ⁻³	3.5×10 ⁻³
\dot{P} = P/τ _{dyn}	9×10 ⁻³	2.8×10 ⁻²
L = E/τ _{dyn} (L _⊙)	5.4	21.6